Supplementary Materials for

Sustainable densification of the deep crust

Benjamin Malvoisin[1,2]*, Håkon Austrheim3, György Hetényi[1], Julien Reynes[4], Jörg Hermann[4], Lukas P. Baumgartner[1], Yury Y. Podladchikov[1]

[1] *Institut des Sciences de la Terre, University of Lausanne, CH-1015 Lausanne, Switzerland.*
[2] *Institut des Sciences de la Terre, Université Grenoble Alpes, CNRS, 38000 Grenoble, France.*
[3] *Physics of Geological Processes, The Njord Centre, Department of geosciences, University of Oslo, 0316 Oslo, Norway.*

[4] *Institute of Geological Sciences, University of Bern, CH-3012 Bern, Switzerland.*

**Correspondence to: benjamin.malvoisin@unil.ch.*

CITATION: Malvoisin, B., et al., 2020, Sustainable densification of the deep crust: Geology, v. 48, https://doi.org/10.1130/G47201.1

This file includes:

Materials and Methods
Figures S1 to S9
Table S2
Captions for Table DR1 and Movies S1 to S2

Other Supplementary Materials for this manuscript include the following:

Table S1
Movies S1 toS2

MATERIALS AND METHODS

Electron microprobe analyses and X-ray mapping

We analyzed mineral composition with a JEOL JXA-8530F HyperProbe at the University of Lausanne equipped with five wavelength dispersive crystal spectrometers (WDS) and one energy dispersive spectrometer (EDS). The machine was operating at 15 keV and 20 nA for garnet and clinopyroxene analyses, at 15 keV and 15 nA for epidote and amphibole analyses and at 10 keV and 10 nA for plagioclase and carbonates analyses. All the analyses were performed with a 1 µm beam diameter except for plagioclase and carbonates for which the beam was defocused to 5 µm to avoid damaging during analysis. The X-ray maps were acquired at a resolution of 10 µm for Figure 1 and 0.68 µm for Supplementary Figure S5 with dwell times of 220 ms and 100 ms, respectively. Reference single point analyses were also acquired to obtain quantitative element distribution and local bulk compositions with the XMapTools software (Lanari et al., 2014).

Electron microprobe analyses of the main minerals are given in Supplementary Table S1.

X-ray microtomography

X-ray computed microtomography of the samples was performed with a SkyScan-1072 at the University of Lausanne. X-ray transmission images were acquired with a rotation step size of 0.225° and an accumulation of 30 frames at two scales, first, on a 4.5 cm diameter drill core with a voxel size of 28 µm and then, after reducing the sample diameter to 0.9 cm, with a voxel size of 6.4 µm.

Determination of H_2O content in nominally anhydrous minerals with Fourier Transform Infrared spectroscopy

Both 360 µm (point analyses) and ~150 µm (maps) thick double polished sections were prepared for Fourier Transform Infrared spectroscopy with a Bruker Hyperion IR microscope at the University of Bern (Switzerland). To limit infrared absorption by air humidity, the sample was flushed with dry air during measurement. Single point measurements were performed with a Mercury-Cadmium-Telluride detector, using 64 scans and a spectral resolution of 4 cm^{-1} using unpolarized light. Absorption maps were acquired with of Focal Plane Array detector collecting 64 x 64 spectra simultaneously. Spectra were corrected for the baseline with the concave rubberband algorithm with three iterations and atmospheric water compensation using the Opus software. They were normalized to 1 cm thickness by using the integral of the garnet overtone between 1650 and 2005 cm^{-1} or the measured thick section thickness for clinopyroxene. For garnet, the signal in the water absorption region was then de-convoluted with Gaussians functions centered at 3416, 3570 and 3650 cm^{-1} corresponding to fluid inclusions, water into

garnet and hydrous phases, respectively. We excluded the spectra for which the area of hydrous phases absorption is superior to 0.15 times the area of the overtone. The area of water into garnet peak was finally converted into H_2O concentration with an absorption coefficient of 2370 L/mol/cm^2 (Maldener et al., 2003). The integrated absorption of clinopyroxene was determined by integrating the absorption signal between 3230 and 3570 cm^{-1}. As we measured with unpolarized light, the total absorbance (sum of absorbance along three perpendicular axes of the absorption indicatrix) was obtained by multiplication by three of the average of the measured unpolarized absorbances (Kovács et al., 2008). Total absorbance was then converted into H_2O concentration with an absorption coefficient for omphacite of 83,400 ± 14,600 L/mol/cm^2 (Katayama et al., 2006).

In addition to the maps provided in Figure 2, infrared absorption spectra and histograms of the water amount distribution are given in Supplementary Figure S7 for garnet and Supplementary Figure S8 for clinopyroxene.

Diffusion-reaction modelling for water content in garnet

We investigated the reaction and diffusion processes potentially responsible for H_2O distribution in garnet with a 2D numerical model. Based on the image acquired for FTIR measurement of H_2O distribution in Figure 2A, the pixels were attributed either to the matrix or to garnet grains. Free fluid is initially present in the matrix at a homogeneous mass concentration of 0.33 wt.% (c). We modelled both its incorporation in the matrix during the precipitation of hydrous minerals and its diffusion into garnet with the following equation:

$$\frac{\partial c}{\partial t} = \nabla(D\,\nabla\, c) - \gamma\frac{\partial \xi}{dt} \qquad (1)$$

where D is the diffusion coefficient of H in garnet for a proton-polaron exchange (10^{-15} m^2.s^{-1} < D < 10^{-13} m^2.s^{-1}; Blanchard and Ingrin, 2004; Kurka et al., 2005; Reynes et al., 2018) and in the fractured and fine-grained plagioclase matrix where it is estimated to be two orders of magnitude higher than in garnet based on intergranular diffusivities estimates (Farver and Yund, 1992). γ is the mass fraction of water in the newly formed hydrous mineral (2 wt.% for epidote here) and ξ is the reaction progress evolving here through time with a first-order reaction rate assuming far from equilibrium conditions:

$$\frac{d\xi}{dt} = r_0\,(1-\xi) \qquad (2)$$

where r_0 is the reaction rate constant in s^{-1}. r_0 values are not available for plagioclase replacement. The rate experimentally determined by Schramke et al. (1987) for K-feldspar + andalusite hydration is 5.9 10^{-6} s^{-1} at 750°C for a grain size of 10 µm. Results of the numerical model with this latter rate and a diffusion coefficient in garnet of 10^{-14} m^2.s^{-1} are given in Figure 2 and Supplementary Figures S3 and S4. The link between D and r_0 values and the reversal of the diffusion profile is investigated in the Supplementary Figure S2.

We used both Neumann (no fluid fluxes at the boundaries; Figure 2 and Supplementary Figure S4) and Dirichlet (constant fluid concentration at the boundaries; Supplementary Figure S3) boundary conditions to test the influence of fluid availability on the results.

Modelling the coupling between reaction, fluid flow and deformation after fluid injection

The 2D model aims at predicting the evolution of porosity and fluid pressure during reaction, fluid flow and deformation. It is based on the equations derived in Malvoisin et al. (2015) and used in (Omlin et al., 2017). The numerical model was benchmarked by reproducing the limits for the purely mechanical and the thermodynamic equilibrium cases (Malvoisin et al., 2015) and an analytical solution for the purely reactive case in a moving coordinate frame (Omlin et al., 2017). We assumed constant total pressure (P_t) and uniform loading (no deviatoric stresses). The main equations are derived from the conservation of solid and fluid momentum, the total and non-volatile components mass conservation and a first-order kinetic law:

$$\nabla \boldsymbol{v_s} = \beta_{et} \frac{dP_f}{dt} - \frac{P_t - P_f}{(1-\phi)\eta_\phi} \quad (3)$$

$$\nabla \frac{k_0 \phi^3}{\eta_f} \left(\nabla P_f + \rho_f g \boldsymbol{e_z} \right) = \beta_{ef} \frac{dP_f}{dt} - \frac{P_t - P_f}{(1-\phi)\eta_\phi} + \left(\frac{\rho_s}{\rho_f} - (1 + \beta_{sr}) \right) \frac{(1-\phi)}{1-X_s} \frac{dX_s}{dt} \quad (4)$$

$$\frac{1}{1-\phi} \frac{d\phi}{dt} = \left(\beta_{et} - \frac{\beta_s' \phi}{1-\phi} \right) \frac{dP_f}{dt} - \frac{P_t - P_f}{(1-\phi)\eta_\phi} - \frac{1+\beta_{sr}}{1-X_s} \frac{dX_s}{dt} \quad (5)$$

$$\frac{dX_s}{dt} = r_0 \left(\frac{\phi}{\phi_0} \right)^{\frac{2}{3}} (X_{seq} - X_s) \quad (6)$$

The variables are the solid velocity, $\boldsymbol{v_s}$, the fluid pressure, P_f, the mass fraction of water into the solid, X_s, and the porosity, ϕ. $\beta_{et} = \beta_d - \beta_s'$ is the effective total compressibility with β_d the drained compressibility (10^{-10} Pa^{-1}) and β_s' the solid compressibility measured in an unjacketed test (3.10^{-11} Pa^{-1}). η_ϕ is the pore effective viscosity. It varies with porosity and effective pressure according to a viscoelastic rheology (Yarushina and Podladchikov, 2015). k_0 is the permeability. η_f is the fluid viscosity (10^{-3} Pa.s). g is the gravity acceleration. ϕ_0 is the porosity at which the reactive surface area is equivalent in rock and powder (a value of 0.38 is used here based on the work of Llana-Fúnez et al., 2007). ρ_f and ρ_s are the fluid and solid densities, respectively. $\beta_{ef} = \beta_{et} + \phi \left(\beta_f - \beta_s' \right)$ is the effective fluid compressibility with β_f the fluid compressibility. β_{sr} is the variation of ρ_s with X_s.

We derived β_f and β_{sr} from ρ_f and ρ_s variations calculated with Gibbs energy minimization at a constant temperature of 750°C (Connolly, 2005). We used as input the bulk system composition (Table S2) determined with the X-ray map acquired at large scale (Figure 1) and XMapTools software (Lanari et al., 2014). X_{seq} is the mass fraction of water into the rock at the equilibrium determined with Gibbs energy minimization and the extent of reaction. r_0 is defined in equation (2) and has the same meaning as in the diffusion-reaction model.

We considered as initial material a granulite with density ($\rho_s = 2900\ kg.m^{-3}$) and composition calculated at equilibrium by Gibbs energy minimization at 800°C and 1.0 GPa (Austrheim and Griffin, 1985; Austrheim, 2013). The equations are solved with an explicit algorithm using pseudotransient iterations (Omlin et al., 2017) on a 100 x 100 Cartesian grid corresponding to a square of 1 x 1 m. We use a Gaussian distribution of porosity with up to 30 % of deviation from this distribution with red noise. No fluxes are allowed at the boundaries to reproduce the closed system conditions observed in the natural samples.

Results of the numerical model are given in Figure 3 as well as in the supplementary materials (Supplementary Movies S1 and S2) for $r_0 = 5.10^{-6}$ s^{-1}, $k = 10^{-19}$ m^2 and $\eta_\phi = 10^{17}$ Pa.s (Schramke et al., 1987; Bürgmann and Dresen, 2008; Ingebritsen, 2012).

We also performed a sensitivity analysis of the model results to the values of r_0, k and η_ϕ. We ran 244 simulations with a 1D model. Each simulation used a different triplet of r_0, k and η_ϕ values. 9 values were probed for r_0 and η_ϕ ranging from 5.10^{-8} to 5.10^{-6} s^{-1} and from 10^{17} to 10^{19} Pa.s, respectively, and 4 values were used for k between 10^{-16} and 10^{-20} m^2. We monitored the minimum fluid pressure and the maximum porosity achieved during each simulation. These two parameters did not vary as a function of k due to no fluid flux as boundary condition. They are thus displayed as a function or r_0 and η_ϕ in the Supplementary Figure S9. We use amphibole precipitation as a criterion to evaluate the parameter values for which the simulations reproduce the observations in the natural sample. This precipitation requires a fluid pressure < 1.65 GPa.

REFERENCES CITED

Austrheim, H., 2013, Fluid and deformation induced metamorphic processes around Moho beneath continent collision zones: Examples from the exposed root zone of the Caledonian mountain belt, W-Norway: Tectonophysics, v. 609, p. 620–635, doi:10.1016/j.tecto.2013.08.030.

Austrheim, H., and Griffin, W.L., 1985, Shear deformation and eclogite formation within granulite-facies anorthosites of the Bergen Arcs, Western Norway: v. 50, p. 267–281.

Blanchard, M., and Ingrin, J., 2004, Hydrogen diffusion in Dora Maira pyrope: Physics and Chemistry of Minerals, v. 31, p. 593–605, doi:10.1007/s00269-004-0421-z.

Bürgmann, R., and Dresen, G., 2008, Rheology of the Lower Crust and Upper Mantle: Evidence from Rock Mechanics, Geodesy, and Field Observations: Annual Review of Earth and Planetary Sciences, v. 36, p. 531–567, doi:10.1146/annurev.earth.36.031207.124326.

Connolly, J.A.D., 2005, Computation of phase equilibria by linear programming: A tool for geodynamic modeling and its application to subduction zone decarbonation: Earth and Planetary Science Letters, v. 236, p. 524–541, doi:10.1016/j.epsl.2005.04.033.

Farver, J.R., and Yund, R.A., 1992, Oxygen diffusion in a fine-grained quartz aggregate with wetted and nonwetted microstructures: Journal of Geophysical Research, v. 97, p. 14017, doi:10.1029/92JB01206.

Ingebritsen, S.E., 2012, Modeling the Formation of Porphyry-Copper Ores: Science, v. 338, p. 1551–1552, doi:10.1126/science.1231706.

Katayama, I., Nakashima, S., and Yurimoto, H., 2006, Water content in natural eclogite and implication for water transport into the deep upper mantle: Lithos, v. 86, p. 245–259, doi:10.1016/j.lithos.2005.06.006.

Kovács, I., Hermann, J., O'Neill, H.S.C., Gerald, J.F., Sambridge, M., and Horváth, G., 2008, Quantitative absorbance spectroscopy with unpolarized light: Part II. Experimental evaluation and development of a protocol for quantitative analysis of mineral IR spectra: American Mineralogist, v. 93, p. 765–778, doi:10.2138/am.2008.2656.

Kurka, A., Blanchard, M., and Ingrin, J., 2005, Kinetics of hydrogen extraction and deuteration in grossular: Mineralogical Magazine, v. 69, p. 359–371, doi:10.1180/0026461056930257.

Lanari, P., Vidal, O., De Andrade, V., Dubacq, B., Lewin, E., Grosch, E.G., and Schwartz, S., 2014, XMapTools: A MATLAB©-based program for electron microprobe X-ray image processing and geothermobarometry: Computers & Geosciences, v. 62, p. 227–240, doi:10.1016/j.cageo.2013.08.010.

Llana-Fúnez, S., Brodie, K.H., Rutter, E.H., and Arkwright, J.C., 2007, Experimental dehydration kinetics of serpentinite using pore volumometry: Journal of Metamorphic Geology, v. 25, p. 423–438, doi:10.1111/j.1525-1314.2007.00703.x.

Maldener, J., Hösch, A., Langer, K., and Rauch, F., 2003, Hydrogen in some natural garnets studied by nuclear reaction analysis and vibrational spectroscopy: Physics and Chemistry of Minerals, v. 30, p. 337–344, doi:10.1007/s00269-003-0321-7.

Malvoisin, B., Podladchikov, Y.Y.Y.Y., and Vrijmoed, J.C.J.C., 2015, Coupling changes in densities and porosity to fluid pressure variations in reactive porous fluid flow: Local thermodynamic equilibrium: Geochemistry Geophysics Geosystems, v. 16, p. 1–57, doi:10.1002/2015GC006019.

Omlin, S., Malvoisin, B., and Podladchikov, Y.Y., 2017, Pore Fluid Extraction by Reactive Solitary Waves in 3-D: Geophysical Research Letters, v. 44, p. 9267–9275, doi:10.1002/2017GL074293.

Reynes, J., Jollands, M., Hermann, J., and Ireland, T., 2018, Experimental constraints on hydrogen diffusion in garnet: Contributions to Mineralogy and Petrology, v. 173, p. 69, doi:10.1007/s00410-018-1492-z.

Schramke, J.A., Kerrick, D.M., and Lasaga, A.C., 1987, The reaction muscovite + quartz andalusite + K-feldspar + water; Part 1, Growth kinetics and mechanism: American Journal of Science, v. 287, p. 517–559, doi:10.2475/ajs.287.6.517.

Yarushina, V.M., and Podladchikov, Y.Y., 2015, (De)compaction of porous viscoelastoplastic media: Model formulation: Journal of Geophysical Research: Solid Earth, v. 120, p. 4146–4170, doi:10.1002/2014JB011258.

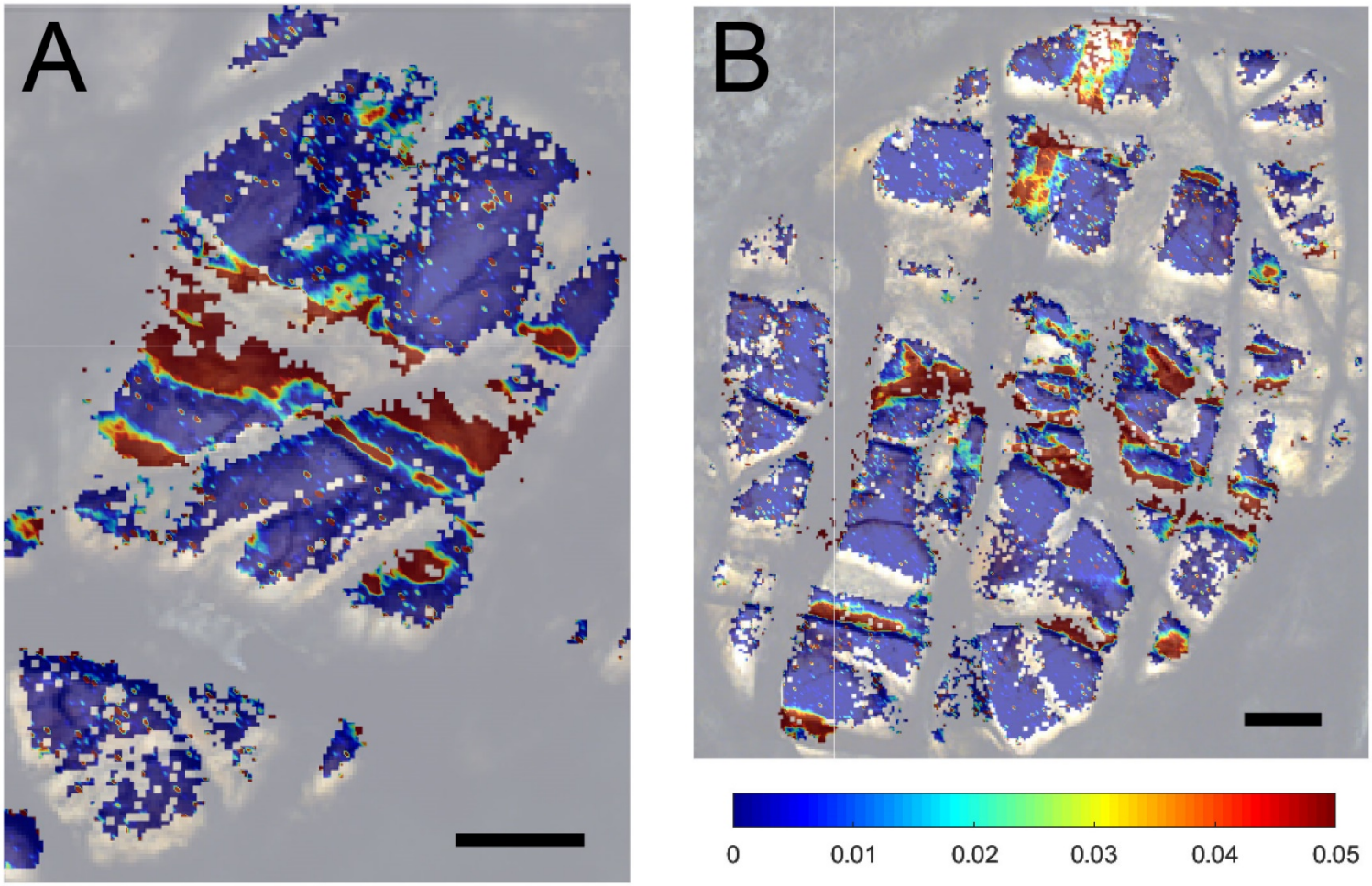

Supplementary Figure S1.

Area of the fluid inclusion peak over area of the garnet overtone peak measured with Fourier Transform Infrared spectroscopy in two grain sets (A and B) found in the vicinity of the pseudotachylyte. The fluid inclusion peak is deconvoluated with a Gaussian centered at 3416 cm^{-1} whereas the overtone peak is taken between 1650 and 2005 cm^{-1}. The scale bar is 200 µm.

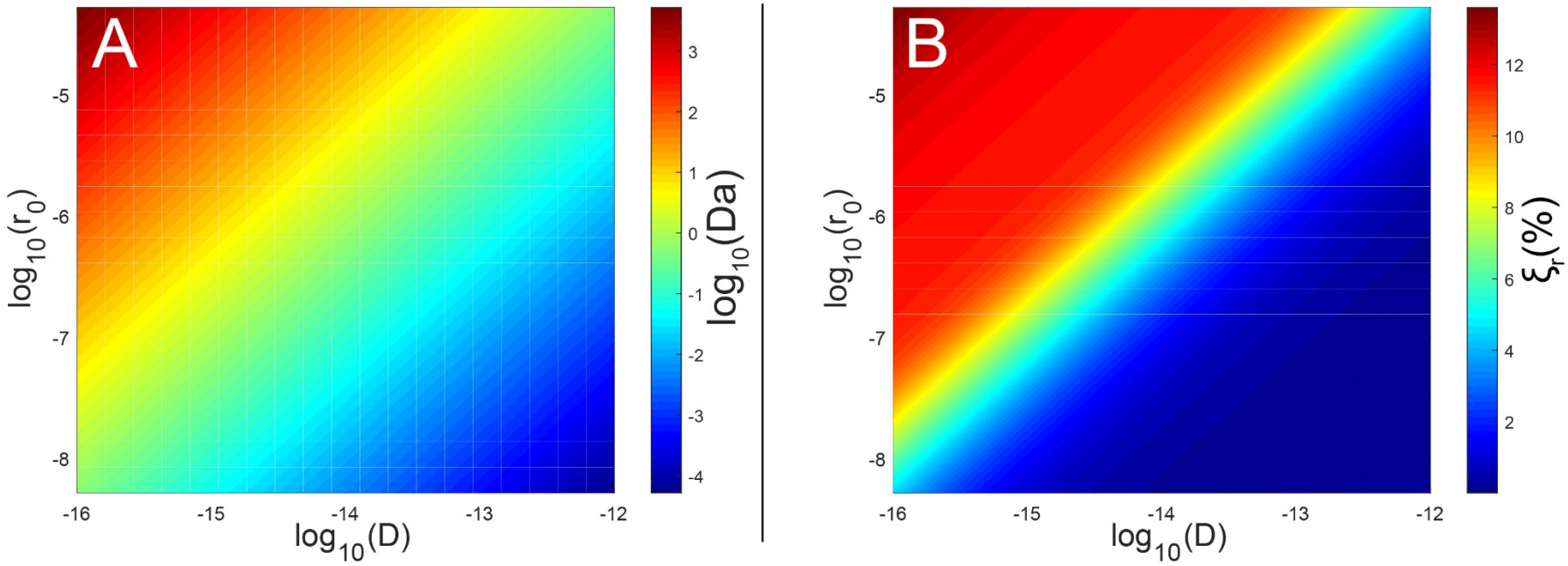

Supplementary Figure DR2.

Sensitivity analysis for the reaction-diffusion model. We investigated the impact of the diffusion coefficient (D in m^2/s) and the reaction rate (r_0 in s^{-1}) values on the reversal of the diffusion profile in a garnet grain in two dimensions with Neumann boundary conditions. The reversal of the profile is defined as the moment when H_2O concentration in the center of the grain becomes higher than H_2O concentration at its rim. A: Damköhler number ($Da = \frac{r_0 L^2}{D}$ with L the characteristic length fixed to 100 µm here) as a function of diffusion coefficient and reaction rate. Da allows to compare the timescales for diffusion and reaction. It is close to one here suggesting that these timescales are similar. B: mean reaction progress in the matrix when the reversal occurs (ξ_r). Note that reversal occurs for all the investigated Da. However, it is not recorded at low Da ($<10^{-2}$) since H_2O concentration in garnet has time to equilibrate with the concentration in the matrix due to fast diffusion compared to reaction. We also investigated the case in which Dirichlet boundary conditions are used, but no reversal was observed before reaction completion.

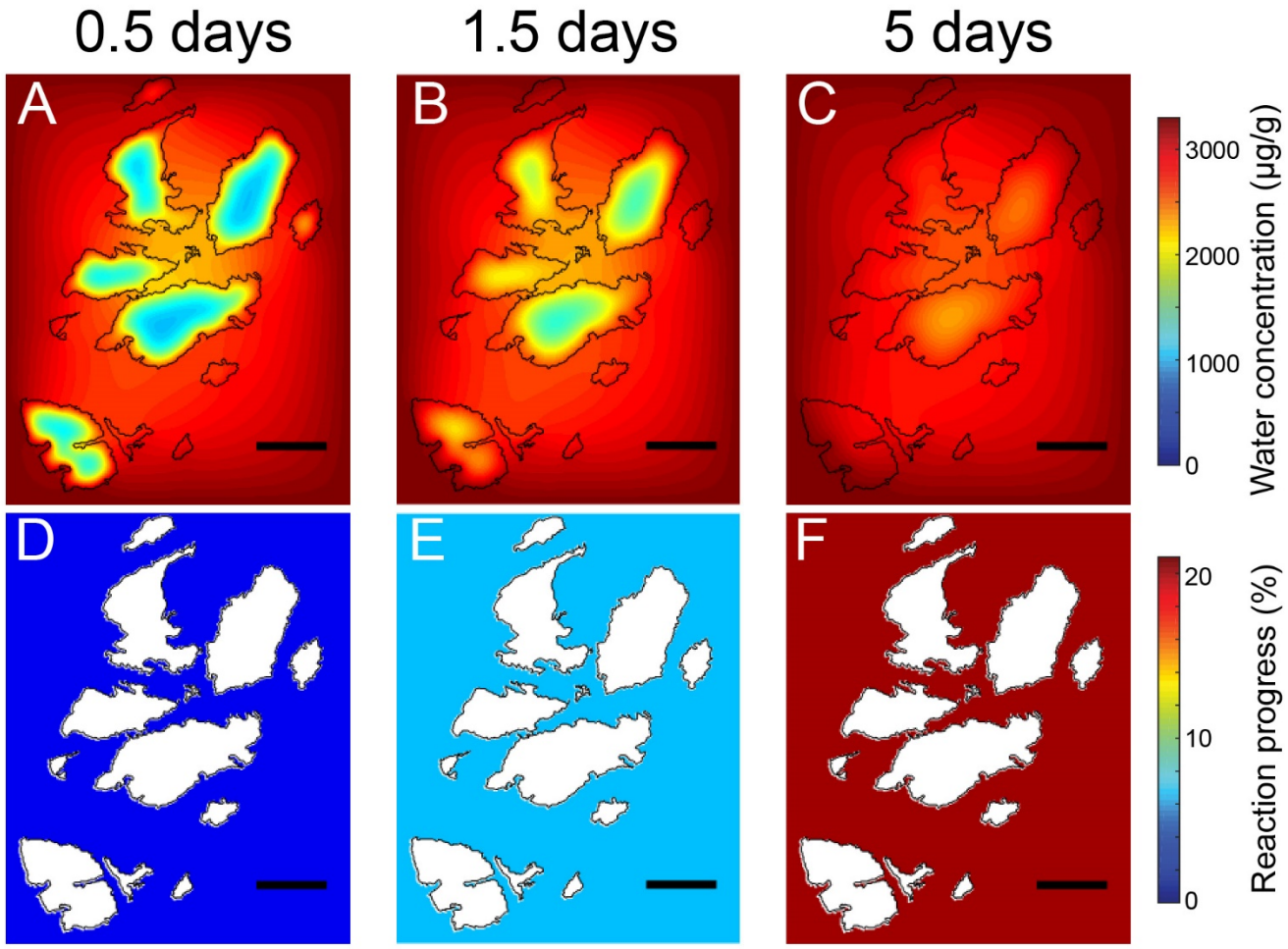

Supplementary Figure S3.
Results of the 2D diffusion-reaction model in a system composed of both garnet grains and a matrix undergoing hydration in open system conditions (Dirichlet boundary conditions with fixed fluid concentration at the boundaries). A to C: prediction of the time evolution of H_2O concentration in garnet and in the matrix. D to F: prediction of the time evolution of reaction progress in the matrix.

In this model, H_2O only diffuses from the matrix into the garnets and reaction products are homogeneously distributed in the matrix. The scale bar is 200 µm.

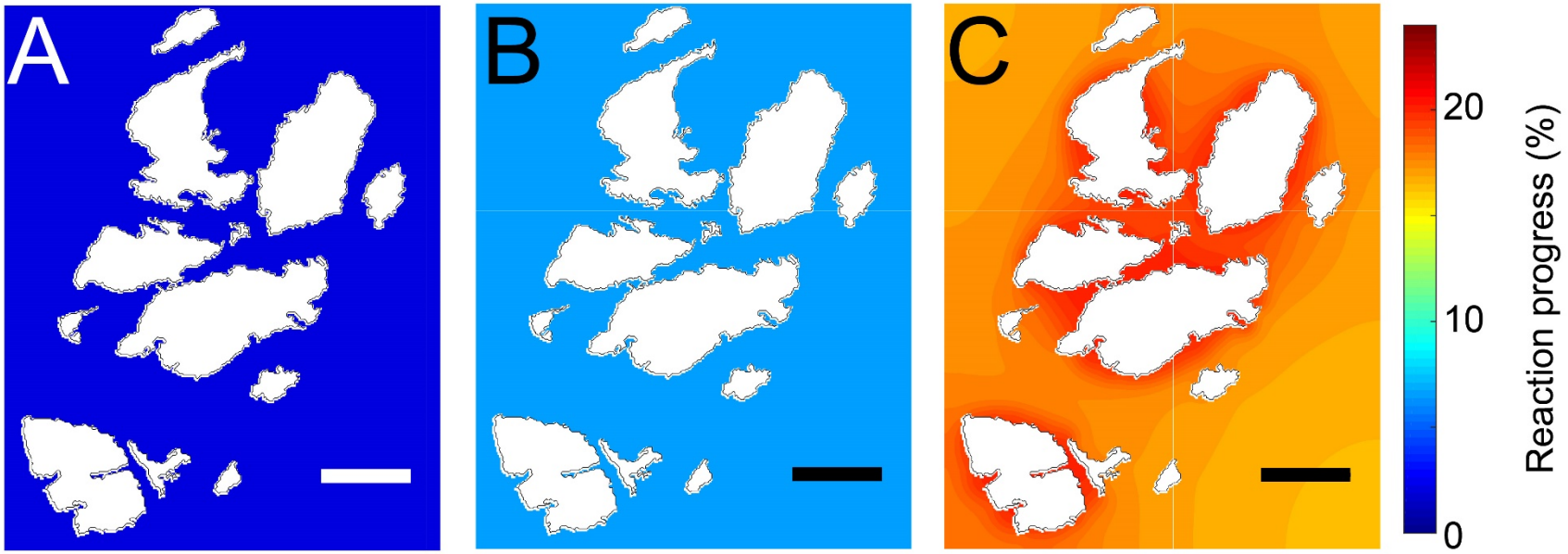

Supplementary Figure S4.

Results of the 2D diffusion-reaction model in a system composed of both garnet grains and a matrix undergoing hydration in a closed system. The time evolution of reaction progress in the matrix is displayed. The scale bar is 200 µm.

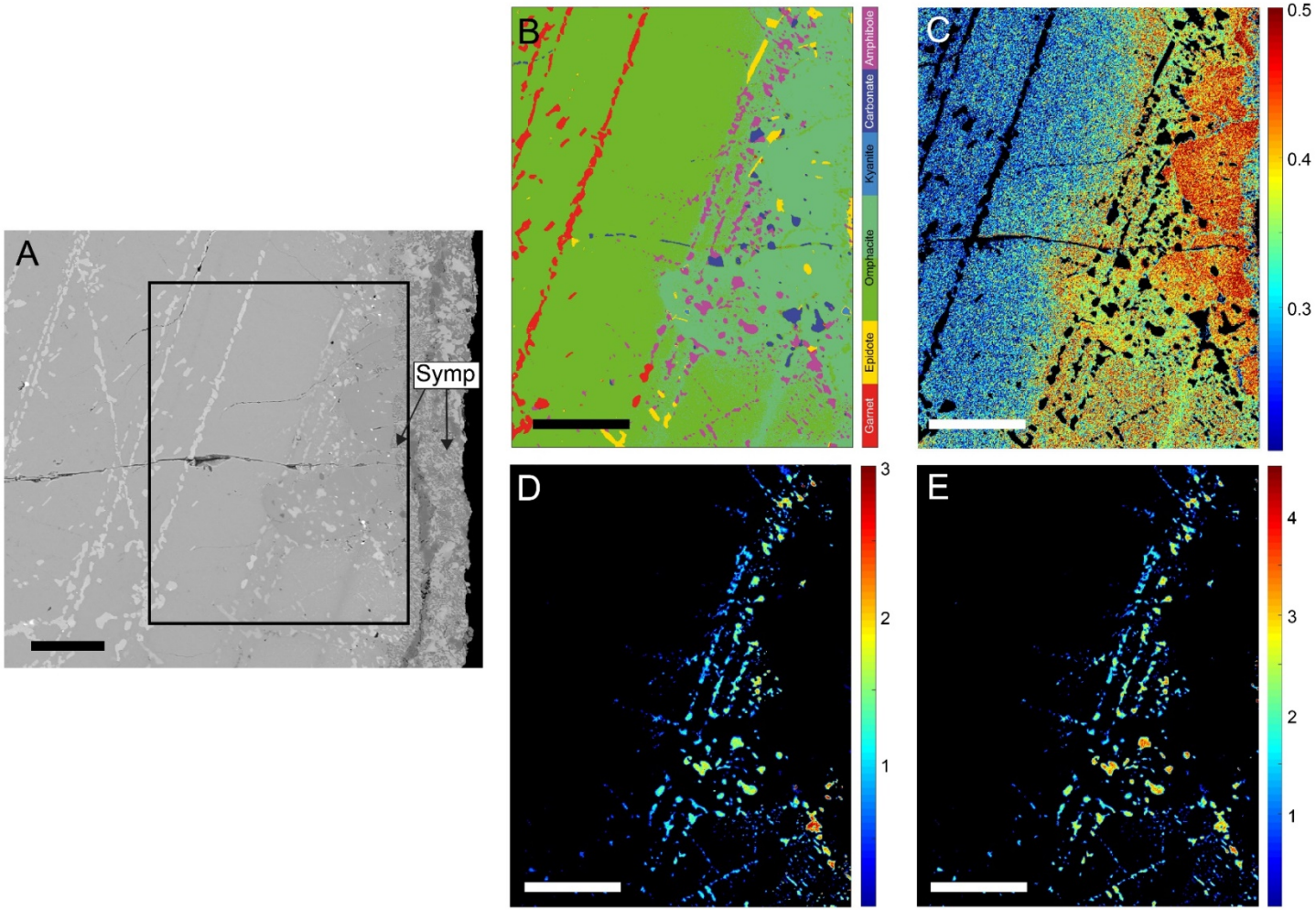

Supplementary Figure S5.
Mineralogical evidence for coupled desiccation and fluid pressure decrease during reaction in sample HKCB_2018_BA7. A: Back-scattered electron image. B: phases identification based on X-ray mapping acquired with the microprobe. Clinopyroxene on the left is replaced at its rim by a sodium-rich clinopyroxene. This latter clinopyroxene is surrounded at its rim by a symplectite made of an intergrowth of plagioclase and diopsidic clinopyroxene (Symp). Minerals of the eclogite facies are found as inclusions in the pyroxene. C: jadeite proportion in pyroxene showing the distribution of the newly formed pyroxene. D: Cl in wt.% in amphibole. E: K_2O in wt.% in amphibole. Note the progressive increase in soluble components in amphibole towards the clinopyroxene rim. Scale bar is 100 µm.

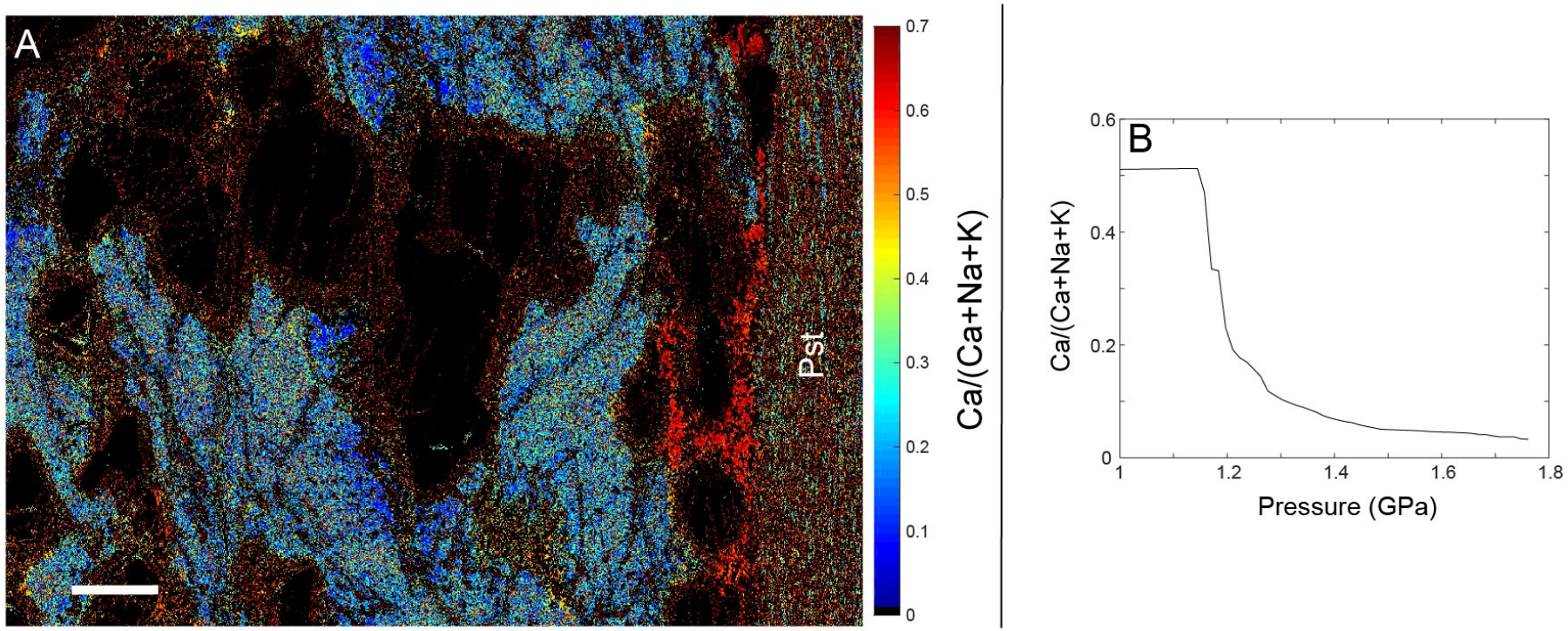

Supplementary Figure S6.

Measured and modelled molar Ca/(Ca+Na+K) ratio in plagioclase. A: Ca/(Ca+Na+K) ratio in plagioclase in sample HKCB_2018_BA7. The ratio was calculated with X-ray maps acquired with microprobe and the XMapTools software (Lanari et al., 2014). Note that plagioclase formed near the pseudotachylyte is enriched in Ca compared to the plagioclases observed in the matrix surrounding the garnet. The scale bar is 1 mm. B: Ca/(Ca+Na+K) ratio as a function of pressure predicted by Gibbs energy minimization. Calculations are performed at 750°C with the local bulk composition given in Supplementary Table DR2. Note the increase in the ratio as the pressure decreases.

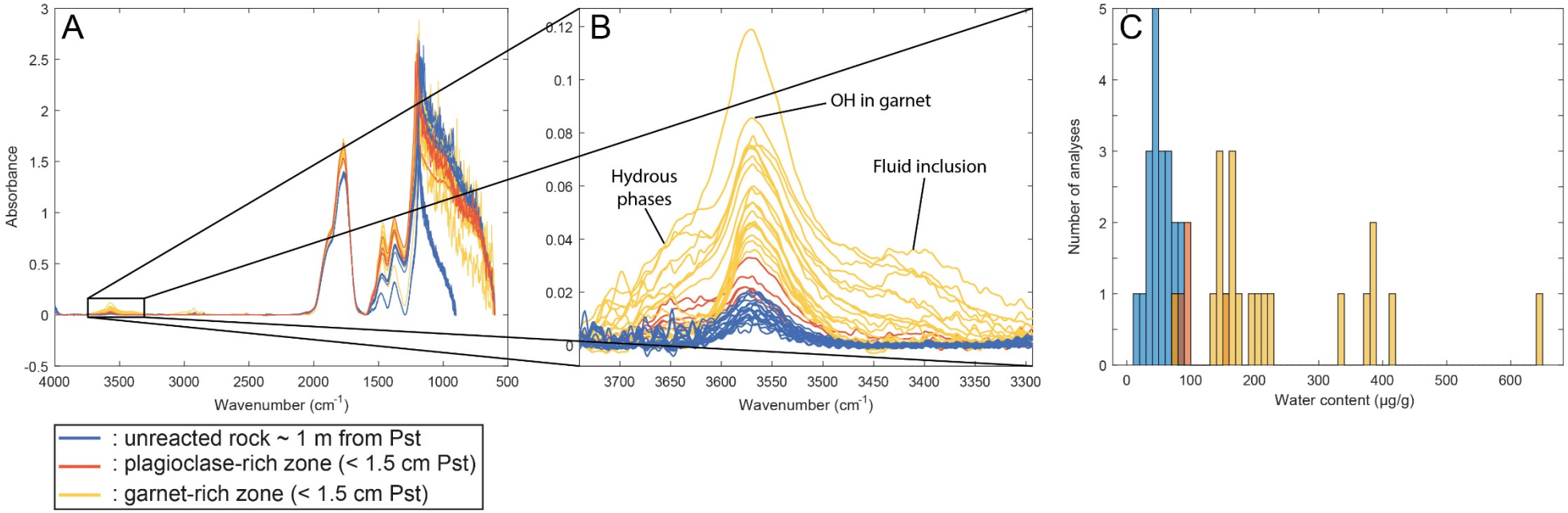

Supplementary Figure S7.

Fourier Transform Infrared spectra acquired in garnets located at different distances from the studied pseudotachylyte. The spectra are normalized to 1 cm thickness. A: whole spectra with garnet overtone between 1650 and 2005 cm^{-1}. B: close-up view in the water absorption region (3290 to 3750 cm^{-1}). The locations of the three peaks used in deconvolution for quantitative analysis are indicated. c: H_2O concentration determined with the absorption coefficient of 2370 L/mol/cm^2 (Maldener et al., 2003).

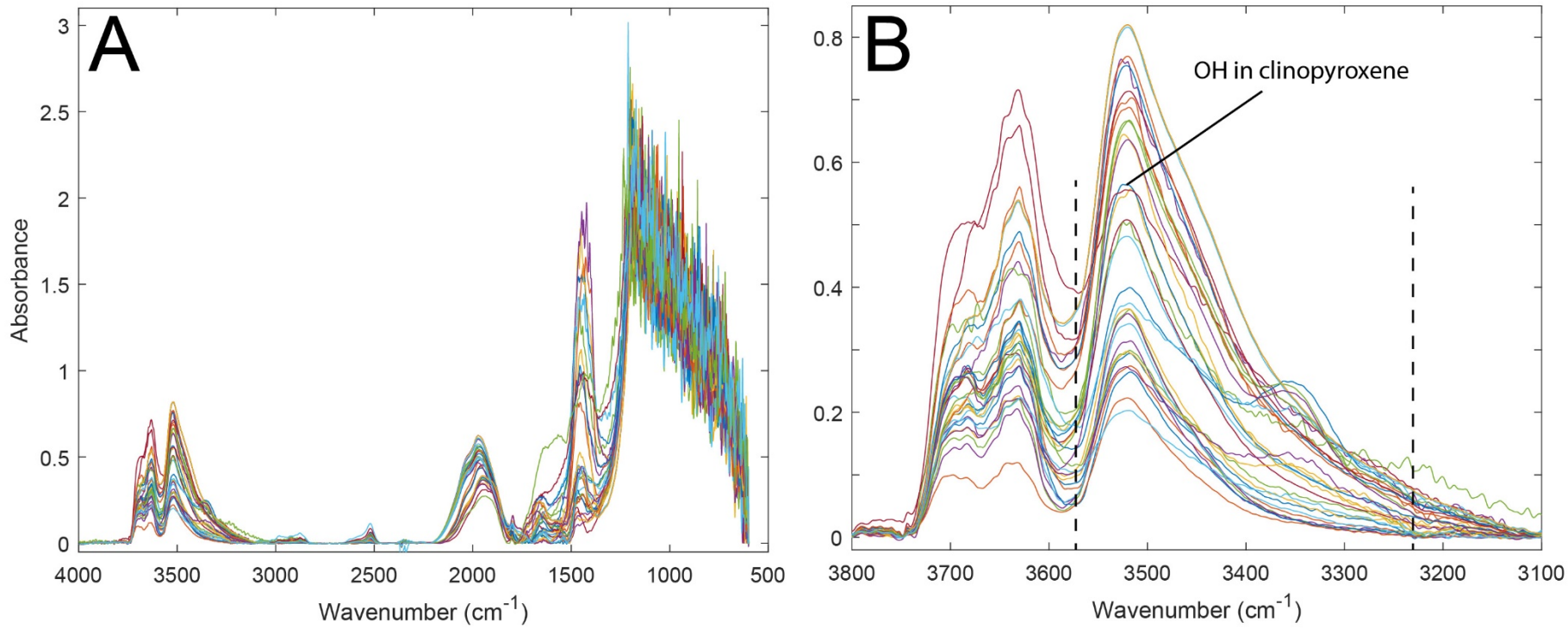

Supplementary Figure S8.

Fourier Transform Infrared spectra acquired in clinopyroxenes located in the vicinity of the pseudotachylyte (< 1 cm). The spectra are normalized to 1cm thickness. A: whole spectra. B: close-up view in the water absorption region. The vertical dashed lines corresponds to the limits used for quantitative analysis of H_2O content into clinopyroxene.

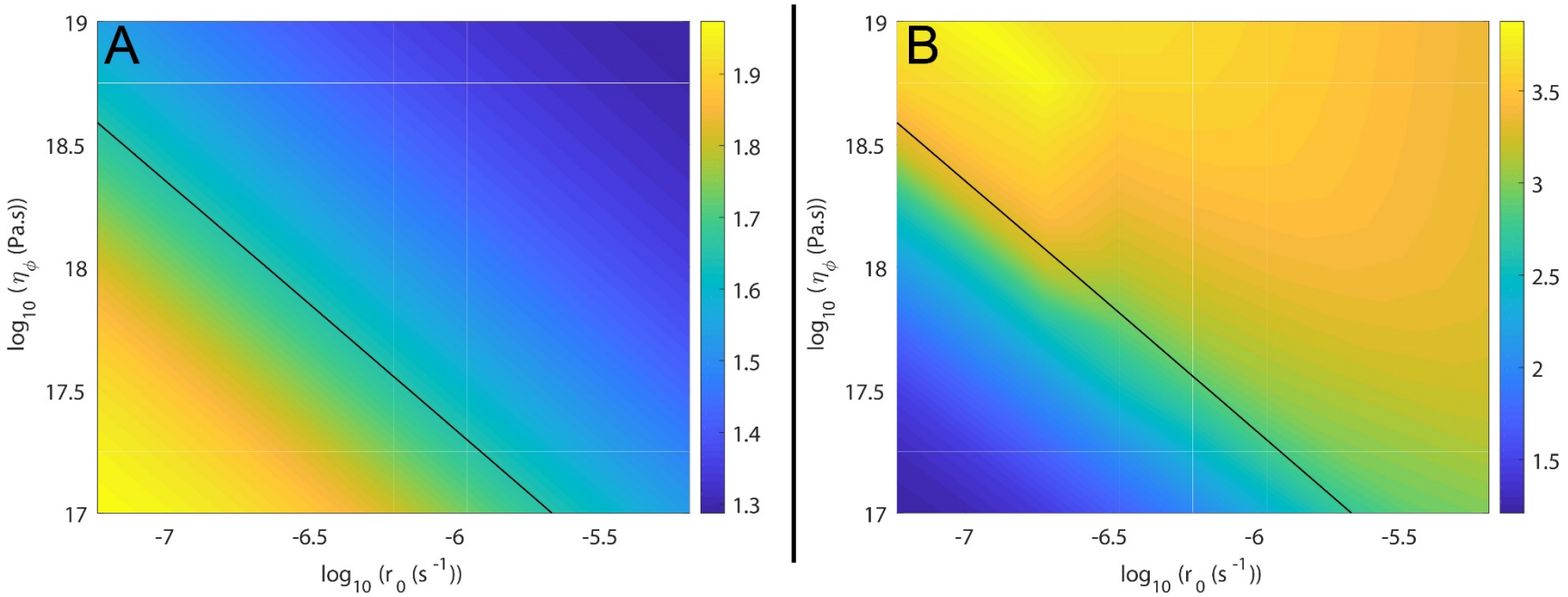

Supplementary Figure S9.

Sensitivity analysis for the numerical model coupling reaction, fluid flow and viscous deformation. Results for 81 simulations are displayed for various reaction rate (r_0) and viscosity (η_ϕ) values. The permeability (k) is fixed to 10^{-19} m^2 in these simulations and does not influence the numerical model results due to the use of no fluid flux as a boundary condition. A: minimum pressure (GPa) achieved during the simulations as a function of r_0 and η_ϕ. B: maximum porosity (%) achieved during the simulations as a function of r_0 and η_ϕ. The black line corresponds to a contour at 1.65 GPa of the minimum calculated pressure.

File Supplementary_Table_S1.xls

Supplementary Table S1.

Representative analyses of garnet, plagioclase, epidote, clinopyroxene and amphibole.

Supplementary Table S2.

Local bulk composition (in wt.%) determined with the X-ray maps acquired on sample BA7 (Figure 1) and the software XMapTools (Lanari et al., 2014). The pseudotachylyte is excluded from local bulk composition calculation. This bulk composition is used for the numerical modelling of the couplings between reaction, deformation and fluid flow.

SiO_2	50.42
TiO_2	0.13
Al_2O_3	23.86
FeO	0.42
Fe_2O_3	4.43
MgO	4.60
MnO	0.09
CaO	10.07
Na_2O	4.28
K_2O	0.31
H_2O	1.38

Supplementary Movie S1.

Evolution of the main parameters in two dimensions as a function of time (in days). Top left panel: fluid pressure. Top right panel: porosity. Bottom left panel: reaction progress. Bottom right panel: proportion of eclogite in the reaction product. Eclogite is the reaction product formed at pressure above 1.77 GPa (top limit of plagioclase stability field). The white crosses correspond to the points where parameters are displayed in Fig. 3.

Supplementary Movie S2.

Evolution of selected mineral modes (vol.%) in two dimensions as a function of time (in days).